Title

Dynamic Rupture Modeling of the M7.2 2010 El Mayor-Cucapah Earthquake: Comparison With a Geodetic Model

Journal

Journal of Geophysical Research: Solid Earth, 122(12)

ISSN

2169-9313

Authors

Kyriakopoulos, C
Oglesby, DD
Funning, GJ
et al.

Publication Date

2017-12-01

DOI

10.1002/2017jb014294

Peer reviewed

Title: Dynamic rupture modeling of the M7.2 2010 El Mayor-Cucapah earthquake: comparison with a geodetic model.

C. Kyriakopoulos[1], D. D. Oglesby[1], G. J. Funning[1] and Kenny Ryan[2]

[1]University of California, Riverside, Department of Earth Sciences.

Geology Building

92521 CA, Riverside, 900 University Ave.

[2]United States Geological Survey, Menlo Park

Contact author: christos@ucr.edu

Keywords: Dynamic Rupture; Multi-fault systems; InSAR; Geodetic Inversions; Topographic effect

Abstract

The 2010 M_w 7.2 El Mayor-Cucapah Earthquake is the largest event recorded in the broader Southern California – Baja California region in the last 18 years. Here we try to analyze primary features of this type of event by using dynamic rupture simulations based on a multi fault interface and later compare our results with space geodetic models. Our results show that, starting from homogeneous prestress conditions, slip heterogeneity can be achieved as a result of variable dip angle along strike and the modulation imposed by stepover segments. We also considered effects from a topographic free surface and find that, although this does not produce significant first-order effects for this earthquake, even a low topographic dome such as the

Cucapah range can affect the rupture front pattern and fault slip rate. Finally, we inverted available InSAR data, using the same geometry as the dynamic rupture model, and retrieved the space geodetic slip distribution that serves to constrain the dynamic rupture models. The one to one comparison of the final fault slip pattern generated with dynamic rupture models and the space geodetic inversion show good agreement. Our results lead us to the following conclusion: in a possible multi-fault rupture scenario, and if we have first order geometry constraints, dynamic rupture models can be very efficient in predicting large scale slip heterogeneities that are important for the correct assessment of seismic hazard and the magnitude of future events. Our work contributes to understanding the complex nature of multi-fault systems.

1. Introduction

The occurrence of multi-fault M>7 events in the last 15 years has stimulated research that aims to better understand the dynamics of large continental earthquakes. These developments are due to two main reasons. First, the collection of new, comprehensive geophysical datasets provides unprecedented and extensive coverage of these events. Second, the rise of supercomputers and advanced numerical techniques allows researchers to simulate large and complex fault ruptures (e.g., Heinecke et al., 2014) that include significant realism such as complex fault geometry and surface topography (e.g., Ely et al., 2010).

In particular, these advances have led to improvements in our ability to simulate dynamic earthquake ruptures with increasing sophistication and detail. A dynamic rupture model is a computational simulation in which initial physical conditions (e.g., the distribution of pre-event stress magnitudes and directions) and assumed physical properties (e.g., friction laws and associated parameters) are applied to a model domain and fault geometry. An earthquake is nucleated when the shear stress on one or more fault elements exceeds its static frictional strength, typically through some sort of artificial nucleation. This simulated earthquake rupture then propagates spontaneously along the model fault surface(s) according to the available stress and any dynamic weakening mechanisms permitted under the friction laws used. In this way, it is possible to gain insights into: the physical conditions under which an earthquake rupture is able to initiate, propagate and ultimately stop; the speed of the fault rupture; the magnitude, rate and distribution of fault slip; and the strong ground motions that accompany the rupture. In the case of a complex multi-segment rupture, we can additionally infer the sequence of events and conditions in which a rupture successfully jumps or otherwise propagates between fault segments (e.g., Harris and Day, 1993; Lozos et al., 2011).

We focus our attention in this study on the M7.2 El Mayor-Cucapah (hereafter 'Cucapah') earthquake, which occurred on at least seven subparallel segments of a fault system extending geographically from the Yuha Desert, southern California at its northern end, across the international border into northern Baja California, Mexico, through the Sierra Cucapah and Sierra El Mayor, and ending within the Colorado River Delta (e.g. Fletcher et al., 2014).

Our interest in this event arises from three main reasons. First, the complex, multi-segment nature of the causative fault system has implications for the physics of the rupture and slip process, and in particular on how we may estimate the potential slip in earthquakes on such structures. Second, this earthquake took place in close proximity to three major fault systems in Southern California (the San Andreas, Imperial, and Elsinore faults), and this event caused triggered earthquakes and slip on these faults to the north. Finally, we note that this event may resemble potential future events in more populated regions in Southern California and elsewhere, where there may be less-characterized fault systems directly adjacent to more well-known ones. The last two times an earthquake of this size hit the Southwestern US/Northwest Mexico were the 1999 M_w 7.1 Hector Mine Earthquake (e.g. USGS, 2000) and the 1992 M_w 7.3 Landers Earthquake (e.g., Hauksson et al., 1993; Olsen et al., 1997), both of which took place on a somewhat analogous systems of non-coplanar fault segments. Fortunately, both of these events and the Cucapah event took place in a less-populated desert environment, but future earthquakes may not be in such fortunate locations.

Although the near-source seismic data coverage is not as good as if the Cucapah event had occurred in a more populated region, it has still been well characterized by multiple data sets, including seismological, geological, space geodetic (InSAR and GPS), geodetic imaging (UAVSAR), and LiDAR. These data have given rise to studies of both the coseismic and postseismic processes for this event, including observations of triggered seismicity and slip in the region (Haukkson et al., 2011; Rymer et al., 2011; Wei, S. et al., 2011; Wei, M. et al, 2011; Graves and Aagaard, [2011];Oskin et al., 2012; Pollitz et al., 2012; Castro et al., 2013; Kroll et al., 2013; Fletcher et al., 2014; Gonzalez-Ortega et al., 2014; Donnellan et al., 2014; Rollins et al., 2015; Spinler et al., 2015; Fletcher et al., 2016; Hines and Hetland [2016]; Huang et al., 2017). The earthquake has been variously characterized as both “superficially simple” (Wei, S. et al., 2011) and “complex” (Fletcher et al., 2016). The differences may arise from the fact that different approaches using different datasets may focus on different aspects of the earthquake and draw different conclusions on its complexity.

The research produced by the various groups can be categorized into two main areas: coseismic and postseismic effects. The global centroid moment tensor (GCMT, www.globalgcmt.org) shows a right lateral strike slip event (M_0=7.62e+19, M_w =7.2) but with a considerable non-double couple component. Prior studies (Hauksson et al., 2011; Wei, S. et al., 2011) indicate that this event nucleated on a N-S oriented normal fault that is adjacent to the main fault system, which could at least partially explain this effect. Wei, S. et al. (2011) also showed that rupture propagated bi-laterally, towards the NW and SE. Models that incorporate geodetic data represent the interface geometry as a concatenation of 4 to 8 faults and with maximum slip between 5 and 6m (Fialko et al., 2010, Wei et al., 2011, Gonzalez-Ortega et al., 2014, Huang et al., 2017). They also show that the majority of slip occurred in the northern region of the fault interface. Studies based on geologic investigations (e.g. Fletcher et al., 2014) and/or studies supported by LiDAR observations (Oskin et al., 2012) highlight the complex rupture pattern of this event, and in particular the activation of several smaller segments near the surface. Postseismic investigations demonstrated the effectiveness of the El Mayor-Cucapah event in triggering seismicity (Kroll et al., 2013) and aseismic slip (Donnellan et al., 2014) on neighboring structures to the north, including the Brawley geothermal area and the San Jacinto fault zone of Southern California (Meng et al., 2014). Furthermore, the first years following the El Mayor-Cucapah event provided the opportunity to study the mechanisms driving the postseismic phase (Gonzalez-Ortega et al., 2014) and allowed investigations of the rheological properties of the local mantle (Pollitz et al., 2012, Rollins et al., 2015, Spinler et al., 2015, Hines and Hetland, 2016).

As our ability increases to model the dynamics of highly complex earthquakes on multiple faults, we must bear in mind that these models must be based on and consistent with actual geophysical data. Therefore, it is useful to combine some sort of data-driven inverse model with the forward dynamic rupture modeling, such as in the case of the 1992 Landers earthquake (Olsen et al., 1997) the 2002 Denali fault earthquake (Oglesby et al., 2004), and the 2010 Haiti earthquake (Douilly et al., 2015). Inverse models can constrain the parameter space of the dynamic models by providing a target for their slip distribution and rupture evolution, and the dynamic models in turn can provide physical insight into the physics underlying the observations.

Our goals are multi-fold. First, we perform 3D dynamic rupture models to investigate the physical sources of the heterogeneous slip pattern of the Cucapah event, including effects from the non-planar, variably-dipping fault geometry and the surface topography. Second, we use geodetic data to infer the slip distribution of the M_w 7.2 2010 El Mayor-Cucapah earthquake. Finally, we investigate how the fault structure and surface topography affect near-source ground motion, with implications for our understanding of fault dynamics and ground motion in general.

2. Methods

a. InSAR Data

The surface rupture of the El Mayor-Cucapah earthquake is covered by four different tracks of the Japanese Aerospace Exploration Agency (JAXA) ALOS PALSAR instrument – two in ascending track geometries and two in descending track geometries (**Figure 1**). Details of these data are given in **Table 1**. We process coseismic interferograms for each of these tracks using the JPL/Caltech ROI_PAC software (Rosen et al., 2004). Topographic artifacts are removed using a 3 arc second digital elevation model from the Shuttle Radar Topography Mission (SRTM; Farr et al., 2007); in each case, the altitude of ambiguity (height change necessary to generate a single fringe) for our interferograms is several times larger than the estimated relative height error for SRTM data in North America (7.0 m), implying that topographic height errors should not be a significant source of error in our data. A branch-cut algorithm (e.g. Goldstein et al., 1988) is used to unwrap the interferometric phase.

To reduce the volume of data to a manageable number of data points, and recognizing the highly correlated nature of InSAR displacement data, we downsample our interferograms using a curvature-based quadtree decomposition (e.g. Simons et al., 2002), specifying a common maximum curvature per quadtree cell. In this way, we reduce the number of data points from millions to ~5700.

b. 3D Finite Element Model

The numerical representation of a complex event such as the M_w 7.2 2010 El Mayor-Cucapah earthquake is a difficult task. The generation of the model geometry presents several challenges that include the implementation of a multi-segment fault surface (**Figure 1**) and an accurate topographic surface. Furthermore, dynamic rupture simulations require the generation of a very dense mesh across the fault interface (in order to resolve rupture propagation). In addition, a mesh algorithm that applies a refinement gradient near the nonplanar fault surface provides computational efficiency. By adding these features to our model, we investigate the effect that a varying dip angle (**Figure 1**) and fault stepovers have on rupture propagation and slip, as well as the effect of accurate topography on both fault slip rate and ground motion.

Our model domain is centered on the Sierra Cucapah mountain range and has dimensions of 160 km X 160 km x 40 km (**Figure 2**). The fault geometry is based on the multi-fault model from Fialko et al., 2010, which is also used in Gonzalez-Ortega et al., 2014 (see table 2 in cited paper). Although it is a simplified version of the complex network of minor faults activated during the 2010 event, this geometry captures first-order fundamental features such as the presence of several fault segments as well as the variation of dip angle along strike. The topography of the model is extracted from the ETOPO1 dataset (Amante and Eakins, 2009) and is down-sampled before the actual model implementation to a discretization of 400m. We anticipate that due to the low altitude of the Sierra Cucapah mountain "dome" (a max height of ~1000m) we would not expect to see first-order effects on the final slip distribution. See **Figure**

S1 for a zoomed in view of the mesh near Sierra Cucapah. However, the detail of our topographic surface (an element size of ~400 m) allows for a thorough investigation of the effects that an irregular free surface can have on the time-dependent rupture process, especially near the surface.

After the fault geometry and surface topography are implemented, our final mesh is composed of approximately ~37 million hexahedral elements. The volume surrounding the fault interface (~1.3km on each side), is meshed with ~133m elements, while for the outer part of the domain the mesh size increases to ~400m. The change of the mesh size away from the fault interface is achieved with the use of a specific refining algorithm that triplicates the size of the hexes while also preserving the quality of the mesh. The software used for the generation of both geometry and mesh is Trelis 15.1 (www.csimsoft.com).

c. Dynamic Rupture Simulations

The complex mesh described in the previous section (**Figure 2**) is the basis for a series of 3D dynamic rupture experiments. We use the finite element code FaultMod (Barrall, 2009). This code allows for the full 3D simulation of dynamic rupture occurring along a fault surface with the coupled off-fault wave propagation, including ground motion. Possible artificial wave reflections from the boundaries of the finite model domain are avoided by using absorbing boundary conditions. FaultMod has been extensively tested and validated under the SCEC/USGS benchmarking exercise (Barall, 2009; Harris et al., 2009). Part of our computations were made using XSEDE supercomputer resources (Towns et al., 2014). A key element in any dynamic rupture simulation is a physical law that describes the evolution of friction as a function of a fundamental parameter such as slip or slip rate. Fault friction has a controlling role in earthquake dynamics, including effects on the stress drop, rupture path, and final slip distribution (e.g., Andrews, 1976; Day, 1982; Harris and Day, 1993; Andrews, 2005; Oglesby et al., 2008). The fault friction law chosen for our experiments is linear slip weakening (e.g., Ida, 1972, Andrews, 1976). A set of initial parameters including the static (μ_{static}) and dynamic ($\mu_{dynamic}$) coefficients of friction and the slip weakening distance d_0 are reported in **Table 2**. The graphical and mathematical representation that synthesizes the linear slip weakening law used here is shown in **Figure** 3 and the following equation:

$$\mu = \begin{cases} \dfrac{\mu_{dynamic} - \mu_{static}}{d_0} \Delta u + \mu_{static}, & \Delta u < d_0 \\ \mu_{dynamic}, & \Delta u \geq d_0 \end{cases}$$

where μ is the frictional coefficient, Δu is the cumulative slip at a location on the fault, and d_0 is the slip weakening parameter.

The nucleation site is near the USGS epicentral location (https://earthquake.usgs.gov/earthquakes/eventpage/ci14607652#executive) of the event, and is approximately in the middle of the fault surface along strike, and at a depth of ~9.5 km. Rupture is allowed for a total length of ~120km along strike. The locking depth is set to be at 20km. The model is initially pre-stressed with constant traction values corresponding to an average presumed stress drop of 2.4MPa under constant normal stress conditions (**Table 1**). The static and dynamic friction coefficients are set to be 0.84 and 0.54 respectively. For simplicity and to allow for a focus on fault geometric and surface topographic effects, we incorporate homogeneous, generic crustal properties (e.g., Mooney et al., 1998) with a Poisson ratio of 0.25 (**Table 2**). To accurately model the earthquake process, our FEM discretization must resolve: (1) the time it takes a P-wave to cross the smallest element dimension, and (2) the breakdown process across rupture front (Palmer and Rice, 1973). Therefore, we check the general (Courant-Friedrichs-Lewy) condition (e.g., Andrews, 1985):

$$\Delta x \geq V_p \Delta t$$

where Δx is the smallest element size, Δt is one time step (that is constant throughout the model duration). Also, we check that the number of elements in the breakdown zone is 4 or more to verify that the stress increase/drop around the rupture front is sufficiently resolved (e.g., Andrews, 2004; Ryan and Oglesby, 2014). Preliminary experiments indicate that a slip weakening parameter of 50cm allows for resolution of the breakdown process, and also allows slip to propagate across the entire fault. Artificial rupture nucleation is achieved by an expanding zone of increased (strike-slip) shear stress within a preset radius of 5 km centered around the simulated hypocenter (see **Figure 4B**); rupture then propagates spontaneously based on the prestress, friction formulation, fault geometry, and material/model properties. Note that we limit the size of the nucleation zone so that artificial nucleation has minimal effects on the slip distribution outside the nucleation region.

3. Dynamic Rupture Simulation Results

a. Dynamic rupture propagation and slip

Our 3D dynamic model produces a complex pattern of rupture propagation and slip that is affected by the fault geometry. In **Figure 4** we show snapshots of stress, slip, and slip rate at representative times for the propagation of rupture. **Figure 4A** shows the model in elastostatic equilibrium (i.e., before nucleation). **Figure 4B** shows the rupture at t=2 s (i.e. 2 seconds after nucleation). In this initial stage of the rupture we see a standard propagating rupture front as seen by perturbations in shear stress, fault slip, and slip rate. There is a roughly circular concentration of shear stress ahead of the crack tip, a concentration of slip rate right behind the crack tip, and a growing patch of slip. There is no change in normal stress at this time since no signal has yet reached the free surface (Oglesby et al., 1998; Oglesby et al., 2000) or any fault areas with complex geometry (e.g., Harris and Day, 1993; Aochi et al., 2002). At t=12 s (**Figure 4B**), the rupture front has now reached the free surface and begun to propagate across two of the fault segments with different dip angles along strike. The combination of the right lateral strike slip motion with the right stepover geometry generates unclamping (i.e., reduces normal stress) of the fault in the stepover region, which facilitates rupture propagating bilaterally towards the north and south. In particular, as rupture approaches the step-over, slip on the main fault unclamps the step-over ahead of it, facilitating propagation through the step-over. Subsequently, slip on the step-over causes clamping along the edges of the main fault segments (adjacent to the step-over), but this effect is not sufficient to terminate rupture. At the same time, shear stress also decreases at the (smaller scale) stepovers because of both the decrease in friction with slip as well as dynamic changes in normal stress. We also see an amplification of the fault slip rate up to values of 2.5m/s as rupture reaches the free surface. At t=20 s (**Figure 4C**), as rupture proceeds in both directions, the slip pattern appears relatively symmetric with respect to the nucleation site and as it was in the previous time snapshot. Rupture propagates around the significant change in dip angle to the south, where the dip changes from vertical to 59 degrees. Fault slip is now above 2.0 m along most of the current rupture surface. At t=40 s after nucleation (**Figure 4D**), rupture has fully developed and slip has reached its final pattern. The final slip and stress pattern emphasizes the importance that fault geometry – an irregular fault interface with varying dip angle – has in our simulations. Although we started our simulation with constant traction values across the fault, the heterogeneity of the final slip distribution is striking. The changes in dip angle as well the unclamping and clamping caused by the step-overs modulates normal and shear stress, and thus generates a slip distribution with variations in both intensity and pattern. Lobes of high and low slip are observed in both the along strike and along dip directions. The maximum value of slip, 5m, occurs at our hypocenter, and is likely affected by our artificial nucleation at that location, with little effect on the slip elsewhere. The final slip distribution is asymmetric, with most slip concentrated on the northern side of the fault and with values greater than 3.75-4m. Maximum values of 3.5m meters are observed south of the nucleation zone. The final slip values correspond to M_0=2.015E+20 Nm (using a 27 GPa shear modulus value), equivalent to a M_w of 7.47. Our preferred dynamic model produces a seismic moment that is larger than that inferred by Hauksson et al., 2011, although it matches our own geodetic model (below) rather well. We could match the seismological moment more precisely through trial and error by downscaling our initial stress values, but instead we choose to focus on the large-scale slip distribution of this event and its time-dependence.

b. Fault slip rate modulation caused by topography

Unlike many such simulations, our dynamic model of the El Mayor-Cucapah event includes an accurate representation of the surface topography. The effect of topography has been previously investigated through point sources and kinematic models and has been shown that might have significant effect in the radiated wavefield (Lee at al., 2009, Ma et al., 2007). We may analyze the effect of the Sierra Cucapah topography on the rupture process by comparing the results to those from an otherwise-equivalent flat topography model. For that reason, we generated an FEM model that shares the exact same fault geometry, material and frictional properties, and stress pattern as the topographic model, but bounded at the top by a flat free surface.

Figures 5, 6, and 7 display comparisons between these experiments. As anticipated earlier, the topography does not have first order effects on fault slip intensity. However, a closer look at the fault slip rate reveals some differences between the flat and topographic models. **Figure 5** compares snapshots of surface particle velocity for these two cases. Nucleation occurs in our model roughly at the center of the simulated fault, near the southern terminus of the Sierra Cucapah range and at the edge of the Colorado River delta area. Rupture then propagates bilaterally and across both the topographic dome of Sierra Cucapah and the flat surface of the delta. For that reason, the NW (left in **Figure 5**) propagating portion of the rupture front will experience effects from topography, while the SE front will primarily travel across a relatively flat surface. At t=7 s (**Figure 5A**) the surface velocity pattern appears to be similar between the two models, although differences in the absolute value are observed, especially as the rupture propagates over the Cucapah range to the left (NW) of the nucleation point. At t=12 and 13 s (**Figures 5B and 5C**), more obvious differences between the two models are observed in the Sierra Cucapah region, while the portion of rupture traveling on the delta shows much less of a difference. Specifically, the presence of topography appears to produce greater ground motion near the rupture front in the Cucapah region, with this motion spread over a larger area. Additional waves are observed propagating throughout the model that appear to be scattered off the topography. At t=25 s (**Figure 5D**), as the rupture front moves away from the highest part of the Cucapah dome (~1000m), the effect of topography decreases and the flat and topographic rupture fronts appear almost identical, but with the continued presence of additional scattered waves in the topographic model.

We note that in the northern reaches of both models, the ground motion pattern is highly asymmetric across the fault due to its dipping geometry (e.g., Oglesby et al., 1998). **Figure 6** provides a summary of the effects of both complex fault geometry and topography on ground motion by comparing the Peak Ground Velocity (PGV) for the topographic and flat model. As explained previously, the major differences are concentrated at the highest parts of Sierra Cucapah (indicated with a black rectangle in **Figure 6**), north of the nucleation point. We observe multiple patches of higher ground motion in this region for the topographic model. To the north (left) of this region, both models show a strong asymmetry in ground motion due to the eastward-dipping fault surface in that area.

An examination of the fault slip rate in the topographic and flat models can shed light on the physical origin of the ground motion differences outlined above. In **Figure 7** we show snapshots of fault slip rate (m/s) for both the flat and topographic models. The largest differences between the slip rate patterns of the flat and topographic models appear to occur beneath the topographic dome, and the intensity of these effects decreases with the reduction in topographic height.

This effect correlates with differences in surface particle velocity between the topographic and flat models as well. We also examine the depth on the fault to which the dynamic rupture is affected by the topographic relief. At t=8 s (**Figure 7A, B**), we observe differences in both the intensity and the spatial pattern of fault slip rate. The topographic model (**Figure 7B**) shows a higher fault slip rate (>2m/s) that is spread over a wider area. We also note additional scattered waves propagating down the fault plane, resulting in a more complex spatial distribution of slip rate. At t=11 s (**Figure 7C, D**), we also note the splitting of the rupture propagation front into two major lobes (**Figure 7D**) instead of the compact front observed in the flat model (**Figure 7C**). Furthermore, the influence of topography on the fault plane appears to extend to at least 5km in depth. Surprisingly, although the maximum height of the Cucapah range is ~1000 m, the depth at which we can still observe its effects is up to five times larger. This observation implies that in other tectonic scenarios with a more prominent topography and higher topographic gradients (e.g. Nepal-Tibet, Wenchuan-China), the affected depth on the fault may be significantly larger.

The effects of topography on rupture propagation and slip can be understood by a simple cartoon visualization of a vertical fault, as shown in **Figure 8**. Seismic waves generated at the rupture front travel ahead of it and are reflected back upon reaching the free surface due to the zero-traction boundary condition there. As predicted by Snell's Law, a seismic wave reaching the Earth's flat free surface (**Figure 8A**) with an incident angle θ_1 will be reflected away by the same angle. For that reason, the flat surface reflects anything other than vertically incident waves away from a vertical fault, leaving no opportunity for the waves to interact with the rupture front. In the topographic model (**Figure 8B**) the surface conditions are different due to the presence of the topographic dome. In this case, a portion of the seismic wave energy can be reflected directly back to the fault and contribute to the rupture and slip process because of a different incident angle with respect to the non-horizontal free surface. Thus, the implementation of a topographic surface in our FEM allows us to observe the interaction of a propagating rupture with waves reflected from the topography. The constructive or destructive interference of the reflected waves is not easy to predict; the stress perturbation inflicted on the fault by the returning waves can lead to a decrease or increase in shear and normal stress depending on the local conditions (e.g., stress perturbations, friction parameterization, topographic geometry, fault geometry etc.).

In spite of these dynamic effects, the low altimetric profile of Sierra Cucapah means that the presence of topography in this specific case is not enough to significantly change the large-scale features of the model, such as the final slip distribution. The final moments of the flat and topographic models are M_0=1.975E+20 Nm (M_w =7.47) and M_0=2.015E+20 Nm (M_w =7.47) respectively and using a 27GPa rigidity value. The difference in moment is something expected and is attributed to the slightly larger fault area of the topographic model (the fault in the topographic model extends above the level of the fault in the flat model beneath the Cucapah dome). The final slip distributions of the two models are also similar, although we do observe some minor differences in slip amplitude in the shallower part of the model in the vicinity of the topographic dome (Supplementary **Figure S2**). This effect is potentially due to differences in the rupture and slip evolution and the slightly larger fault area in the topographic model. The differences observed in fault slip rate, especially the shallower part of the fault, suggest that a mountain range of large area and greater relief could play an important role in the evolution of rupture.

c. Effects of Variations of the initial model setup

To better understand how changes in basic parameters might affect the outcome of the final slip pattern, we tested additional models. We specifically investigated the effect of shallower locking depth (15 and 18km instead of 20km) and lower static (0.6 instead of 0.84) and dynamic (0.10 instead of 0.54) friction coefficient values. Results from these additional experiments are presented in Supplementary **Figures S3** and **S4**. The locking depth appears to control the intensity of final slip values and the final seismic moment, a direct consequence of the reduction in available rupture area. The estimated seismic moment drops from M_0=2.015E+20 Nm (M_w =7.47) in the 20km locking depth case to M_0=1.708E+20 Nm (M_w =7.43) for the 18km locking depth and M_0=1.253E+20 Nm (M_w =7.34) for the 15km locking depth case. As before, the shear modulus is set to 27GPa. We should also note that in the top two models (18 and 20km) the overall pattern is asymmetric with higher slip values to the north, while this pattern is not so clear in the 15km locking depth case. We also tested a model with a higher presumed fractional stress drop (2.7MPa) by using μ_{static} = 0.6 and $\mu_{dynamic}$ = 0.1 and with decreased initial stress values (shear stress = 3.5MPa, normal stress = 7.9MPa). **Figure S4** shows a comparison of the two cases. The first and most striking difference is that in this new simulation the higher concentration of slip occurs north of the nucleation location (at 60km along strike), whereas in the original case slip decreased progressively towards the northern termination of the fault. The final moment for the high fractional stress drop model is M_0=2.25E+20 (M_w=7.5). Although the final slip pattern appears asymmetric as in the original case, the gradient in the observed seismic slip has changed and now is increasing towards north. In addition, the slip pattern in this high fractional stress drop case is less heterogeneous than in our preferred model.

4. Geodetic model

a. InSAR inversion for slip

The main goal of the geodetic inversion presented in this section is to provide a data-driven fault slip distribution that can then be physically interpreted with respect to our dynamic modeling. In particular, InSAR-based geodetic models provide spatial constraints on fault slip that can be used to analyze geometrically complex multi-segment events. The InSAR datasets used in this study provide a wide coverage on both the near and far deformation field of the Cucapah event. The linear inversion is based on a combination of FEM generated Green's functions (GF's), homogeneous medium with poisson ratio of 0.25, and the surface displacement field detected by four different ALOS tracks. The final product is a final slip map that we can use for comparisons with our dynamic rupture model. The finite element model used for the generation of the GF's utilizes the same fault geometry as the dynamic rupture model, although the mesh density required for the elastostatic model is significantly lower. The geodetic model is implemented in a larger semi-spherical domain (radius = 1200km), with the fault positioned in the center (see

Figure S5). We rely on the much larger size of the elastostatic model (10 times the size of the fault) to avoid boundary effects on the static deformation filed.

The final mesh is composed of approximately 800,000 hexahedral elements. The mesh size is 1.5 km near the fault, and smoothly becomes larger (up to 60km) towards the boundaries and the bottom of the semi-sphere. This transition is implemented via a bias scheme that spreads radially from the center domain were the fault is implemented. The fault interface is divided into 44 along-strike and 9 along-dip coincident nodes (patches) with an average size of 3 x 3 km, for a total of 396 patches. The elementary elastostatic solution-response (GF's) for each of these patches is generated in a manner similar to previous work by Masterlark (2003), Kyriakopoulos and Newman (2016), and Kyriakopoulos et al. (2013), using the commercial finite element code ABAQUS (simulia.com). These elementary responses are calculated for both the along strike and dip directions, and are later used to populate our GF matrix, the core of our linear inversion. We use a general least squares inversion scheme with smoothing and right lateral positivity constraints based on the Matlab lsqlin function. Our final slip model is extracted through an iterative process (**Figure 9B to D**), comparing solutions with increasing roughness and lower residuals as described in Jonsson et. al, 2002. Our model is calibrated to simultaneously fit the four InSAR ALOS datasets (tracks t211, t212, t532 and t533). Our selected slip model is shown in **Figure 9B**. Modeled and observed InSAR points are presented in **Figure S6** and **S7**.

The overall slip pattern appears to be asymmetric from north to south. More specifically, the northern part of the fault is characterized by slip values greater than 3.0m (large orange to red slip area between 60-100km along strike) distributed at depths shallower than 9-10km. In the southern part, the slip intensity decreases to values between 2-3 m. The only exception consists on a secondary concentration of slip at the southern end of the fault model (at 140km along strike), with maximum slip of 3-3.5 m. The larger slip values correspond with the steep part of the fault (dip angles of 71-79 degrees). The maximum depth of significant (>1.5 m) slip varies between 5 and 18km as we move from north to south. A smaller concentration of slip, separated from the main rupture, is also observed at the northern end of the fault (between 20-40km along strike) on a somewhat deeper part of the fault interface. This feature is likely to be the result of noise in the data or artifacts of an orbital ramp included in the ALOS data. The geodetic moment estimated using the slip distribution from our preferred model, with shear modulus equal to 27GPa, is M_0=1.759E+20 N m, equivalent to M_w=7.43, higher than the M_w 7.2 estimated with seismological methods. However, this value drops to M_0=0.652E+20 N m, equivalent to M_w 7.15, if we use a 10GPa shear modulus value that characterizes better the shallower and less compacted rocks. Finally, if instead we use an average 20GPa, the final moment is M_0=1.303E+20 Nm, equivalent to M_w 7.35. In general, the larger moment is likely due to two main factors: a slip concentration in the deeper part related to orbital ramps and noise in the data, and the inclusion of aseismic afterslip in the geodetic model.

b. Comparison between the dynamic and geodetic models

Dynamic rupture simulations and geodetic models provide us with complementary approaches for the study of earthquake slip in the Cucapah event, with the dynamic forward model being based on a small number of physical assumptions, and the inverse geodetic model based on data and a different set of physical assumptions. For the dynamic rupture model, we assume in advance the prestress values, the friction law, and the fault geometry. The inverse geodetic model also depends on the choice of basic parameters such as the fault geometry, as well as the choice of constraints (e.g. positivity, smoothing) within the inversion algorithm. The dynamic rupture model produces a time-dependent solution based on the evolution of the friction law, while the InSAR geodetic model is essentially static because it is based on the acquisition of pre- and a post-earthquake radar images. The dynamic method is a fundamental tool to understand underlying fault rupture processes, whereas the geodetic model provides constraints and validation. The complementarity of these two methods motivates us to use them independently and compare their results. We specifically compare the geodetic model with the dynamic rupture model bounded by the flat free surface, since our geodetic model does not include topography.

The two models show a significant first order agreement, especially in the main segments, while slip in the step overs is less similar. The common features can be summarized as follows: 1) Slip appears asymmetrically distributed in both cases, with higher slip to the north; 2) The maximum slip values range between 4-5 m; 3) The majority of slip appears concentrated above 10km depth; 4) In the main segments, the location of high slip patches appear to correspond in the two models. For example, the high slip in both models is between 60-100km along strike; 5) The final seismic moment is similar ($M_0^{drupt\_flat}$=1.975E+20 Nm and M_0^{geod} = 1.759E+20 Nm) if we use for our calculation a 27GPa shear modulus. Conversely, the main differences include: 1) The dynamic rupture model shows higher slip values (green color) at depth between 40-60km and 100-120km along strike; 2) Slip depth variations are stronger in the geodetic model, although this is affected by the weight of smoothing; 3) Slip in the step-over segments of the fault is higher in the dynamic rupture model. This is the unavoidable effect of the assumed constant traction.

5. Discussion and Conclusions

Other works before ours presented estimates of the slip distribution for the El Mayor-Cucapah event (Fialko et al., 2010, Wei, S. et al., 2011, Gonzalez-Ortega et al., 2014, Huang et al., 2017). The datasets used to constraint the final slip include teleseismic waveforms, InSAR points, GPS measurements, SPOT images and/or various combinations of these. Furthermore, although the fault geometry used in these works captures similar and essentials features (e.g. the changing in dip angle near the epicentral area and strike orientation) some differences are present. Details in the datasets, inversion method used and fault geometry makes the direct comparison difficult, however the evaluation of large scale features is still possible. For example, all the above models place the majority of slip in the northern part of the modeled interface, which also coincides with the steeper part of their fault model and the max slip values fall between 4-6 m. These are all features also present in both our dynamic rupture model and geodetic inversion.

Our models indicate that both the fault geometry and free surface topography of the El Mayor-Cucapah event likely produced effects on the rupture dynamics of this earthquake, including significant stress and slip rate perturbations. In particular, slip on the fault produces dynamic changes in shear and normal stress on non-coplanar fault segments, leading to a complex rupture process and a heterogeneous slip distribution. Additionally, the free surface scatters the stress waves in a somewhat unpredictable manner. There may be a complex relationship between the fault geometry and surface topography that we cannot evaluate in this study.

A main result of our current work is that a dynamic model that includes accurate fault geometry can reproduce first order features of the inferred slip pattern in this earthquake. Importantly, our dynamic model did not require a complicated heterogeneous pre-stress field to reproduce the large-scale heterogeneous slip pattern. If true and if generalizable to other events, this result is good news for the prediction of fault slip distribution in future events, as the geometry of faults is much more likely to be constrained than the initial stress pattern. Many more earthquakes will need to be analyzed in this way to determine if such a statement can definitely be made; indeed, earlier work that pairs dynamic models to slip inversions (e.g., Oglesby *et al.*, 2004) may indicate that additional stress complexity may be necessary to explain slip patterns in very large events such as the 2002 Denali Fault event.

Some caveats to this work are in order. In the dynamic model, our nucleation takes place on the main rupture surface. As demonstrated in previous studies (Hauksson et al., 2011; Wei, S. et al., 2011), the earthquake did not start on one of the main NW-SE oriented faults that slipped in this event (Passo Superior, Borrego, Pescadores, Indiviso), but rather nucleated on an adjacent N-S oriented normal fault that crosses the central sector of the main segment near the estimated epicenter. For simplicity, our model does not include this effect, although it would likely have only a minor effect on our overall slip pattern and details of rupture propagation. Nonetheless, future studies should focus on identifying these small faults near larger structures, and determining how a potentially larger earthquake could be triggered by the smaller faults. Additionally, we use a uniform shear and normal prestress distribution, so we have not investigated the effects from heterogeneous prestress distributions on the rupture dynamics (although as noted above, we reproduce the geodetic slip relatively well regardless). Finally, we used homogeneous material properties in both our models to isolate the effects of fault geometry. However, we arguing that this assumption does not strongly affect our comparison between the geodetic and dynamic models, since vertical and lateral inhomogeneities will similarly affect estimates of slip in both the dynamic and static cases.

There have been few studies on dynamic rupture modeling using regional topographic data.

Specifically, Ely et al., 2010 showed that the topographic surface might have an effect on the rupture process and ground motion. Furthermore, based on Zhang et al., 2016, topography appears to affect the sub-shear to supershear transition. Our current work shows how topography may break up and intensify the rupture front with implications for ground motion. The effect of near-fault topography is something that bears additional study beyond this current work. We plan to systematically investigate geometric factors of surface topography in relation to rupture dynamics at stepovers in the future.

Acknowledgements

The authors gratefully acknowledge FaultMod developer Michael Barall (Invisible Software) for his considerable help and continuous support for this project. We also want to thank John Fletcher (CICESE) and Jennifer Tarnowski (UCR) for many useful conversations. Keith Richards-Dinger provided computing support with the local cluster. This research was funded by the National Science Foundation (NSF) grants EAR-1114446 and EAR-1135455. This work used the Extreme Science and Engineering Discovery Environment (XSEDE), which is supported by National Science Foundation grant ACI-1548562; specifically, the Comet cluster at the San Diego Supercomputer Center (SDSC). ALOS data are copyrighted by JAXA, and were supplied via an agreement with the Alaska Satellite Facility. Figures were made with GMT (Wessel et al., 2013) and PARAVIEW (www.paraview.org). All aerial photograph imagery (**Figures 2,4 and S1**) from Google Earth (https://www.google.com/earth/). The dynamic rupture and geodetic model results are available upon request from the first author.

Table 1: Details of ALOS PALSAR interferogram data used in this study.

Track	Geometry	Frames	Incidence[a]	Date 1	Date 2	$B_\perp$ (m)[b]	h_a (m)[c]	N[d]
211	Ascending	620–650	34.3°	2010/01/15	2010/04/17	744	80	1341
212	Ascending	620–640	34.3°	2009/12/17	2010/05/04	-972	61	2495
532	Descending	950–970	34.3°	2009/02/10	2010/05/16	-2846	21	927
533	Descending	950–970	34.3°	2009/11/30	2010/04/17	-1415	42	973

[a]Radar incidence angle at interferogram center

[b]Perpendicular baseline at interferogram center

[c]Altitude of ambiguity at interferogram center

[d]Number of quadtree-sampled data points

Table 2: Material and modeling properties.

τ_o initial shear stress (MPa)	18
σ_o initial normal stress (MPa)	29
τ_{nuc} nucleation stress (MPa)	25
Static friction	0.84
Dynamic friction	0.54
Slip weakening distance (m)	0.5
Density (kg/m^3)	2700

Poisson ratio	0.25
S-wave speed (m/s)	3162
P-wave speed (m/s)	5477
Nucleation radius (m)	5000
Nucleation speed (m/s)	2000
Fault element Size (m)	~133
Off-fault element size (m)	~400
Rupture time step (s)	10^-2

References

Amante, C. and Eakins, B. W. (2009). ETOPO1 1 Arc-Minute Global Relief Model: Procedures, Data Sources and Analysis. NOAA Technical Memorandum NESDIS NGDC-24. National Geophysical Data Center, NOAA. doi:10.7289/V5C8276M.

Andrews, D. J. (1976). Rupture velocity of plane strain shear cracks. Journal of Geophysical Research, 81(32), 5679-5687.

Andrews, D. J. (1985). Dynamic plane-strain shear rupture with a slip-weakening friction law calculated by a boundary integral method. Bulletin of the Seismological Society of America, 75(1), 1-21.

Andrews, D. J. (2004). Rupture models with dynamically determined breakdown displacement. Bulletin of the Seismological Society of America, 94, 769–775.

Andrews, D. J. (2005). Rupture dynamics with energy loss outside the slip zone, J. Geophys. Res., 110, B01307, doi:10.1029/2004JB003191.

Aochi, H., Madariaga, R., and Fukuyama, E. (2002). Effect of normal stress during rupture propagation along nonplanar faults. *Journal of Geophysical Research: Solid Earth*, *107*(B2), doi:10.1029/2001JB000500.

Barall, M. (2009). A grid-doubling finite-element technique for calculating dynamic three-dimensional spontaneous rupture on an earthquake fault. Geophysical Journal International, 178(2), 845-859.

Castro, R., J. Acosta, V. Wong, A. Perez-Vertti, A. Mendoza, and L. Inzunza (2011), Location of aftershocks of the 4 April 2010 Mw 7.2 El Mayor-Cucapah earthquake of Baja California, Mexico, Bull. Seismol. Soc. Am., 101(6), 3072–3080.

Day, S. M. (1982). Three-dimensional finite difference simulation of fault dynamics: rectangular faults with fixed rupture velocity. Bulletin of the Seismological Society of America, 72(3), 705-727.

Donnellan, A., J. Parker, S. Hensley, M.Pierce, J. Wang, and J. Rundle (2014), UAVSAR observations of triggered slip on the Imperial, Superstition Hills, and East Elmore Ranch Faults associated with the 2010 M 7.2 El Mayor-Cucapah earthquake, Geochem. Geophys. Geosyst., 15, 815–829, doi:10.1002/2013GC005120.

Douilly, R., Aochi, H., Calais, E. & Freed, A.M., 2015. Three-dimensional dynamic rupture simulations across interacting faults: the Mw7.0, 2010, Haiti earthquake, *Journal of Geophysical Research,* 120**,** 1108-1128.

Ely, G. P., Day, S. M., and J. B. Minster (2010). Dynamic rupture models for the southern San Andreas fault. *Bulletin of the Seismological Society of America*, *100*(1), 131-150.

Farr, T. G., P. A. Rosen, E. Caro, R. Crippen, R. Duren, S. Hensley, M. Kobrick, M. Paller, E. Rodriguez, L. Roth, D. Seal, S. Shaffer, J. Shimada, J. Umland, M. Werner, M. Oskin, D. Burbank, and D. Alsdorf (2007). The Shuttle Radar Topography Mission, Reviews of Geophysics, 45, RG2004, doi:10.1029/2005RG000183.

Fialko, Y., A. Gonzalez, J. Gonzalez, S. Barbot, S. Leprince, D. Sandwell, and D. Agnew (2010), Static rupture model of the 2010 Mw 7.2 El Mayor-Cucapah earthquake from ALOS, ENVISAT, SPOT and GPS data, Abstract T53B-2125 presented at 2010 Fall Meeting, AGU, San Francisco, Calif.

Fletcher, J. M, Michael E. Oskin and Orlando J. Teran, The role of a keystone fault in triggering the complex El Mayor–Cucapah earthquake rupture, Nature Geoscience 9, 303–307 (2016) doi:10.1038/ngeo2660.

Fletcher, J. M., et al. (2014), Assembly of a large earthquake from a complex fault system: Surface rupture kinematics of the 4 April 2010 El Mayor-Cucapah (Mexico) Mw 7.2 earthquake, Geosphere, 10, 797–827, doi:10.1130/GES00933.1.

Goldstein, R. M., H. A. Zebker, and C. Werner (1988), Satellite radar interferometry: Two-dimensional phase unwrapping, Radio Sci., 23, 713 – 720.

Gonzalez-Ortega, A., Y. Fialko, D. Sandwell, F. A. Nava-Pichardo, J. Fletcher, J. Gonzalez-Garcia, B. Lipovsky, M. Floyd, and G. Funning (2014), El Mayor-Cucapah (Mw 7.2) earthquake: Early near-field postseismic deformation from InSAR and PGS observations, J. Geophys. Res. Solid Earth, 119, 1482–1497, doi:10.1002/2013JB010193.

Graves, R. W. and B. T. Aagaard (2011, April), Testing long-period ground-motion simulations of scenario earthquakes using the Mw 7.2 El Mayor-Cucapah mainshock: Evaluation of finite-fault rupture characterization and 3D seismic velocity models, Bulletin of the Seismological Society of America, 101(2), 895-907, doi: 10.1785/0120100233.

Harris, R. A., and Day, S. M. (1993). Dynamics of fault interaction: Parallel strike-slip faults. Journal of Geophysical Research: Solid Earth, 98(B3), 4461-4472.

Harris, R. A., Barall, M., Archuleta, R., Dunham, E., Aagaard, B., Ampuero, J. P., Bhat, H., Cruz-Atienza, V., Dalguer, L., Dawson, P., Day, S., Duan, B., Ely, G., Kaneko, Y., Kase, Y., Lapusta, N., Liu, Y., Ma, S., Oglesby, D., Olsen, K., Pitarka, A., Song, S., and Templeton, E. (2009). The SCEC/USGS dynamic earthquake rupture code verification exercise. Seismological Research Letters, 80(1), 119-126.

Hauksson, E., L. M. Jones, K. Hutton, and D. Eberhart-Phillips (1993), The 1992 Landers Earthquake Sequence: Seismological observations, J. Geophys. Res., 98(B11), 19835–19858, doi:10.1029/93JB02384.

Hauksson, E., J. Stock, K. Hutton, W. Yang, J. A. Vidal-Villegas, and H. Kanamori (2011), The 2010 Mw 7.2 El Mayor-Cucapah earthquake sequence, Baja California, Mexico and Southernmost California, USA: Active seismotectonics along the Mexican Pacific margin, Pure Appl. Geophys., 168, 1255–1277, doi:10.1007/s00024-010-0209-7.

Hauksson, E. and W. Yang, and P.M. Shearer, "Waveform Relocated Earthquake Catalog for Southern California (1981 to 2011)"; Bull. Seismol. Soc. Am., Vol. 102, No. 5, pp.2239-2244, October 2012, doi: 10.1785/0120120010

Heinecke, A., Breuer, A., Rettenberger, S., Bader, M., Gabriel, A. A., Pelties, C., ... & Smelyanskiy, M. (2014). Petascale high order dynamic rupture earthquake simulations on heterogeneous supercomputers. In Proceedings of the International Conference for High Performance Computing, Networking, Storage and Analysis, 3-14, IEEE Press.

Hines, T. T., and E. A. Hetland (2016), Rheologic constraints on the upper mantle from 5 years of postseismic deformation following the El Mayor-Cucapah earthquake, J. Geophys. Res. Solid Earth, 121, 6809–6827, doi:10.1002/2016JB013114.

Huang, M.-H., E. J. Fielding, H. Dickinson, J. Sun, J. A. Gonzalez-Ortega, A. M. Freed, and R. Bürgmann (2017), Fault geometry inversion and slip distribution of the 2010 Mw 7.2 El Mayor-Cucapah earthquake from geodetic data, J. Geophys. Res. Solid Earth, 122, 607–621, doi:10.1002/2016JB012858.

Ida, Y. (1972). Cohesive force across the tip of a longitudinal-shear crack and Griffith's specific surface energy. Journal of Geophysical Research, 77(20), 3796-3805.

Jónsson, S., Zebker, H., Segall, P., & Amelung, F. (2002). Fault slip distribution of the 1999 Mw 7.1 Hector Mine, California, earthquake, estimated from satellite radar and GPS measurements. Bulletin of the Seismological Society of America, 92(4), 1377-1389.

Kroll, K. A., E. S. Cochran, K. B. Richards-Dinger, and D. F. Sumy (2013), Aftershocks of the 2010 Mw 7.2 El Mayor-Cucapah earthquake reveal complex faulting in the Yuha Desert, California, J. Geophys. Res. Solid Earth, 118, 6146–6164, doi:10.1002/2013JB010529.

Kyriakopoulos, C., T. Masterlark, S. Stramondo, M. Chini, and C. Bignami (2013), Coseismic slip distribution for the Mw 9 2011 Tohoku-Oki earthquake derived from 3-D FE modeling, J. Geophys. Res. Solid Earth, 118, 3837–3847, doi:10.1002/jgrb.50265.

Kyriakopoulos, C., and A. V. Newman (2016), Structural asperity focusing locking and earthquake slip along the Nicoya megathrust, Costa Rica, J. Geophys. Res. Solid Earth, 121, 5461–5476, doi:10.1002/2016JB012886.

Lee, Shiann-Jong, et al. (2009), Effects of topography on seismic-wave propagation: An example from northern Taiwan, Bulletin of the Seismological Society of America 99.1, 314-325.

Lozos, J. C., D. D. Oglesby, B. Duan, and S. G. Wesnousky (2011), The effects of fault bends on rupture propagation: a geometrical parameter study, Bulletin of the Seismological Society of America, 101(1), 385-398.

Ma, S., R. J. Archuleta, and M. T. Page (2007). Effects of large-scale surface topography on ground motions, as demonstrated by a study of the San Gabriel Mountains, Los Angeles, California, Bull. Seismol. Soc. Am.97, 2066 – 2079, doi 10.1785/0120070040.

Magistrale H, Lucile Jones and Hiroo Kanamori, The Superstition Hills, California, Earthquakes of 24 November 1987 (1989), BSSA, Vol.79, No.2,pp.239-251, April 1989.

Masterlark, T. (2003), Finite element model predictions of static deformation from dislocation sources in a subduction zone: Sensitivities to homogeneous, isotropic, Poisson-solid, and half-space assumptions, J. Geophys. Res., 108(B11), 2540, doi:10.1029/2002JB002296.Mooney, W. D., Laske, G., and Masters, T. G. (1998). CRUST 5.1: A global crustal model at 5× 5. Journal of Geophysical Research: Solid Earth, 103(B1), 727-747.

Oglesby, D. D., Archuleta, R. J., and Nielsen, S. B. (1998). Earthquakes on dipping faults: the effects of broken symmetry. Science, 280, 1055–1059.

Oglesby, D. D., Archuleta, R. J., and Nielsen, S. B. (2000). The three-dimensional dynamics of dipping faults. Bulletin of the Seismological Society of America, 90, 616–628.

Oglesby, D.D., Dreger, D., Harris, R.A., Ratchkovski, N.A. & Hansen, R., 2004. Inverse kinematic and forward dynamic models of the 2002 Denali Fault Earthquake, Alaska, *Bulletin of the Seismological Society of America,* 94**,** S214-S233.

Oglesby, D. D., P. M. Mai, K. Atakan, and Pucci, S. (2008), Dynamic models of earthquakes on the North Anatolian fault zone under the Sea of Marmara: Effect of hypocenter location, Geophys. Res. Lett., 35, L18302, doi:10.1029/2008GL035037.

Olsen, K.B., Madaraiga, R. & Archuleta, R.J., 1997. Three-dimensional dynamic simulation of the 1992 Landers earthquake, *Science*, 278**,** 834-838.

Oskin, M. E., et al. (2012), Near-field deformation from the El Mayor-Cucapah earthquake revealed by differential lidar, Science, 335, 702–705, doi:10.1126/science.1213778.

Palmer, A. C., and Rice, J. R. (1973). The growth of slip surfaces in the progressive failure of over-consolidated clay. In Proceedings of the Royal Society of London A: Mathematical, Physical and Engineering Sciences (Vol. 332, No. 1591, pp. 527-548). The Royal Society.

Pollitz, Fred F., Roland Bürgmann, and Wayne Thatcher, Illumination of rheological mantle heterogeneity by the M7. 2 2010 El Mayor-Cucapah earthquake, Geochemistry, Geophysics, Geosystems 13.6 (2012).

Rollins, Christopher, Sylvain Barbot, and Jean-Philippe Avouac. "Postseismic deformation following the 2010 M= 7.2 El Mayor-Cucapah earthquake: Observations, kinematic inversions, and dynamic models." Pure and Applied Geophysics 172.5 (2015): 1305-1358.

Rosen, P. A., S. Henley, G. Peltzer, and M. Simons (2004), Updated Repeat Orbit Interferometry Package Released, Eos Trans. AGU, 85(5), 47.

Ryan, K. J., and Oglesby, D. D. (2014). Dynamically modeling fault step overs using various friction laws. Journal of Geophysical Research, 119(7), 5814–5829.

Rymer, M. J., et al. (2011), Triggered surface slips in Southern California associated with the 2010 El Mayor-Cucapah, Baja California, Mexico earthquake, U.S. Geol. Surv. Open File Rep. 2010-1333 and Calif. Geol. Surv. Spec. Rep. 221, 62 pp. [Available at http://pubs.usgs.gov/of/2010/1333/.].

Southern California Earthquake Center. Caltech. Dataset. doi:10.7909/C3WD3xH1

Spinler, J. C., R. A. Bennett, C. Walls, L. Shawn, and J. J. G. Garcia (2015), Assessing long-term postseismic deformation following the M7.2 4 April 2010, El Mayor-Cucapah earthquake with implications for lithospheric rheology in the Salton Trough, J. Geophys. Res. Solid Earth, 120, 3664–3679, doi:10.1002/2014JB011613

Towns, J., Timothy Cockerill, Maytal Dahan, Ian Foster, Kelly Gaither, Andrew Grimshaw, Victor Hazlewood, Scott Lathrop, Dave Lifka, Gregory D. Peterson, Ralph Roskies, J. Ray Scott, Nancy Wilkins-Diehr (2014), XSEDE: Accelerating Scientific Discovery, Computing in Science & Engineering, vol.16, no. 5, pp. 62-74, Sept.-Oct. 2014, doi:10.1109/MCSE.2014.80

U.S. Geological Survey and California Geological Survey, 2006, Quaternary fault and fold database for the United States, accessed Apr 6, 2017, from USGS web site: https://earthquake.usgs.gov/hazards/qfaults/.

US Geological Survey, Southern California Earthquake Center, and California Division of Mines and Geology. Preliminary report on the 16 October 1999 M 7.1 Hector Mine, California, earthquake. Seismol. Res. Lett. 71, 11-23 (2000).

Wei, M., D. Sandwell, Y. Fialko, and R. Bilham (2011), Slip on faults in the Imperial Valley triggered by the 4 April 2010 Mw 7.2 El Mayor-Cucapah earthquake revealed by InSAR, Geophys. Res. Lett., 38, L01308.

Wei, S., et al. (2011), Superficial simplicity of the 2010 El Mayor-Cucapah earthquake of Baja California in Mexico, Nat. Geosci., 4, 615–618.

Wessel, P., W. H. F. Smith, R. Scharroo, J. Luis and F. Wobbe (2013), Generic Mapping Tools: Improved Version Released, Eos Trans. AGU, 94(45), 409.

Zhang, Z., J. Xu, and X. Chen (2016), The supershear effect of topography on rupture dynamics, Geophys. Res. Lett., 43, 1457–1463, doi:10.1002/2015GL067112.

Figures Captions

Figure 1. Sierra Cucapah region. The surface projection of the model fault interface is highlighted in purple. Aftershocks of the 2010 El-Mayor Cucapah are shown as green circles with transparency [Hauksson et al., 2012]. The orange colored curves represent fault segments based on Fialko et al. [2010]. The names of the faults are extracted from Gonzalez-Ortega et al. [2014]; 1-Paso Superior, 2-Paso Inferior accommodation zone (PIAZ), 3-Borrego (first half) and La Puerta accommodation zone (PAZ), 4-Pescadores, 5-Pescadores (first half) and Indiviso, 6-7, Indiviso. A 3D representation of these segments is shown in **Figure 2c**. Red curves show known surface ruptures in the US side (Imperial, Superstition Hills and Coyote Creek faults, U.S. Geological Survey database). The thick yellow line shows the US-Mexico border. The USGS estimated epicenter is marked with a yellow star. Four different InSAR ALOS tracks are shown with blue color symbols: t211 continuous line, t212 dots and dashes, t532 dots and t533 dashes.

Figure 2. Mesh of the finite element model and fault geometry. (A) View of entire finite element mesh. (B) Close-up view of the mesh around the fault interface. (C) Fault segments (see Figure 1 caption for more info) used to generate the underlying continuous fault interface (individual faults are ultimately connected when modeled).

Figure 3. Schematic representation of friction coefficient versus slip for linear slip-weakening friction. The friction coefficient μ drops from the static coefficient of friction μ_s to the dynamic coefficient of friction μ_d over a slip distance of d_0. The final slip is denoted by d_f.

Figure 4. View of dynamic rupture simulation, including topography, at t=2, 12, 20 and 40 s. Each subplot is composed of four panels showing the time evolution of (starting from the top left

and moving clockwise) Fault Slip (m), Normal Stress (MPa), Shear Stress (MPa), and Fault Slip Rate (m/s). View is approximately from the NE to the SW.

Figure 5. (Map View) Surface particle velocity (m/s). Comparison between the topographic and flat models. Time snapshots are at (A) t=7 s, (B) t=12 s, (C) t=13 s, and (D) t=25 s.

Figure 6. (Map View) Peak Ground Velocity (PGV). (A) View of the entire flat model and (C) zoomed-in view; (B) View of the entire topographic model and (D) zoomed-in view. The black box highlights the zoomed-in area of major differences between the two models.

Figure 7. View from approximately SW towards NE of fault slip rate (m/s) for flat (left column) and topographic (right column) models at (A-B) t=8 s, (C-D) t=11 s. The black continuous lines running across the fault surface represent depth contours at 5, 10, 15, 20 km. The along-strike fault distance is highlighted by white vertical lines (every 20km).

Figure 8. Schematic representation of ray wave paths and the influence of a non-flat free surface. (A) Flat model; (B) Topographic model. Note that waves are scattered differently in each case.

Figure 9. Slip distributions from dynamic rupture and geodetic models. (A) Dynamic rupture model; (B) Selected geodetic model; C) to D) smoother geodetic models. The horizontal black lines correspond to 5km depth contours. Vertical black lines show 20km intervals along strike starting from the northwestern end of the fault. View from approximately SW towards NE.

Figure 1.

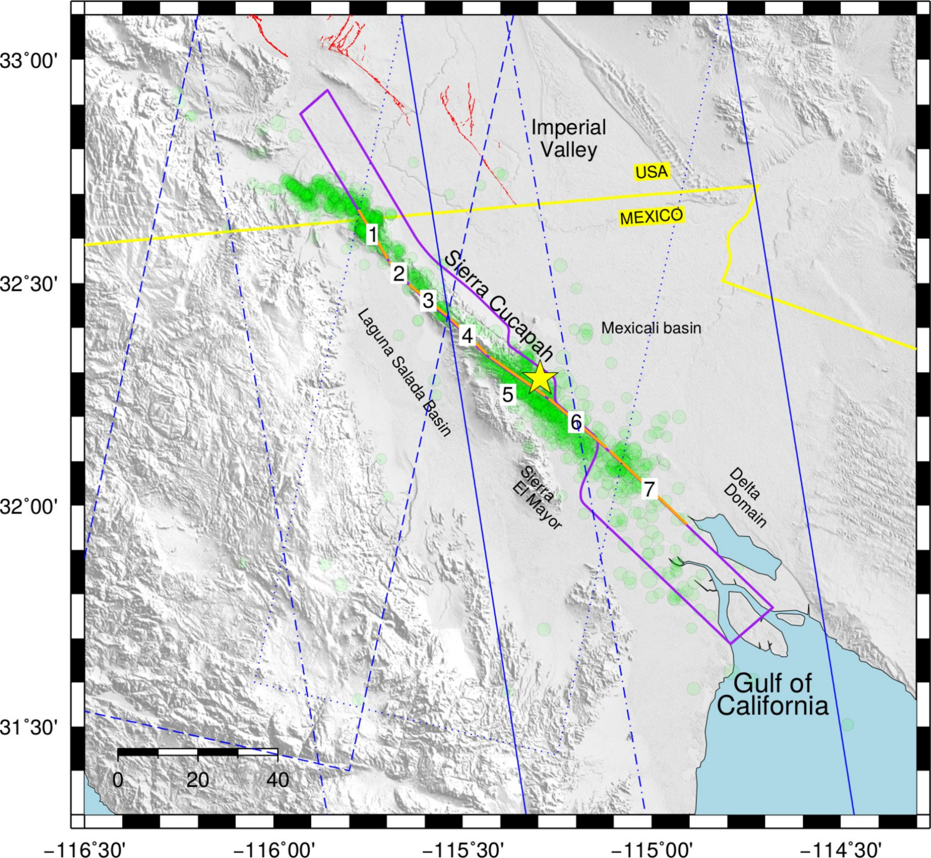

33°00'
32°30'
32°00'
31°30'
−116°30'
−116°00'
−115°30'
−115°00'
−114°30'
Imperial Valley
USA
MEXICO
Sierra Cucapah
Mexicali basin
Laguna Salada Basin
Sierra El Mayor
Delta Domain
Gulf of California
1
2
3
4
5
6
7
0
20
40

Figure 2.

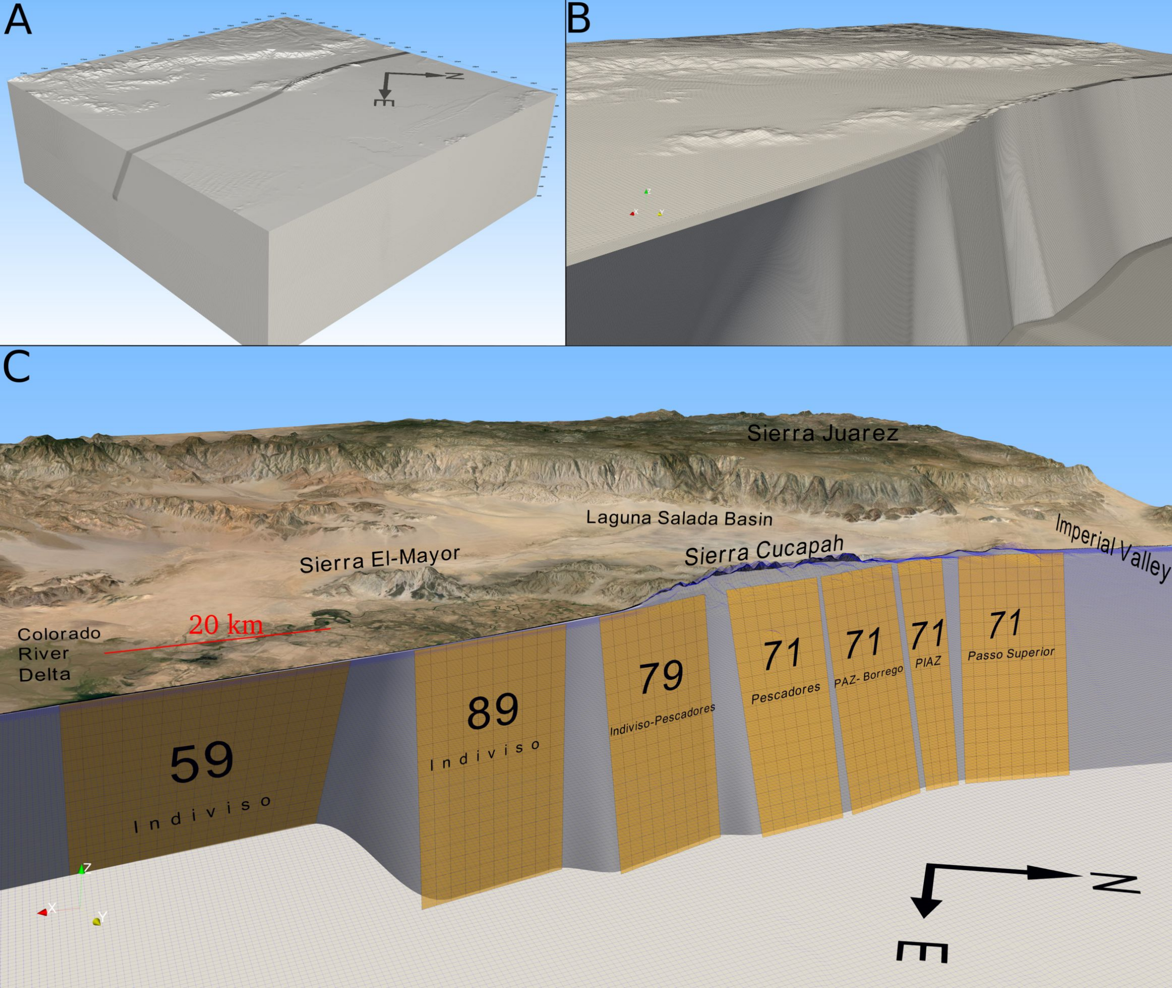

A
B
C
Sierra Juarez
Laguna Salada Basin
Imperial Valley
Sierra Cucapah
Sierra El-Mayor
20 km
Colorado River Delta
59
Indiviso
89
Indiviso
79
Indiviso-Pescadores
71
Pescadores
71
PAZ- Borrego
71
PIAZ
71
Passo Superior
N
E

Figure 3.

friction coefficient μ
μ_s
μ_d
d_0
d_f
slip u

Figure 4.

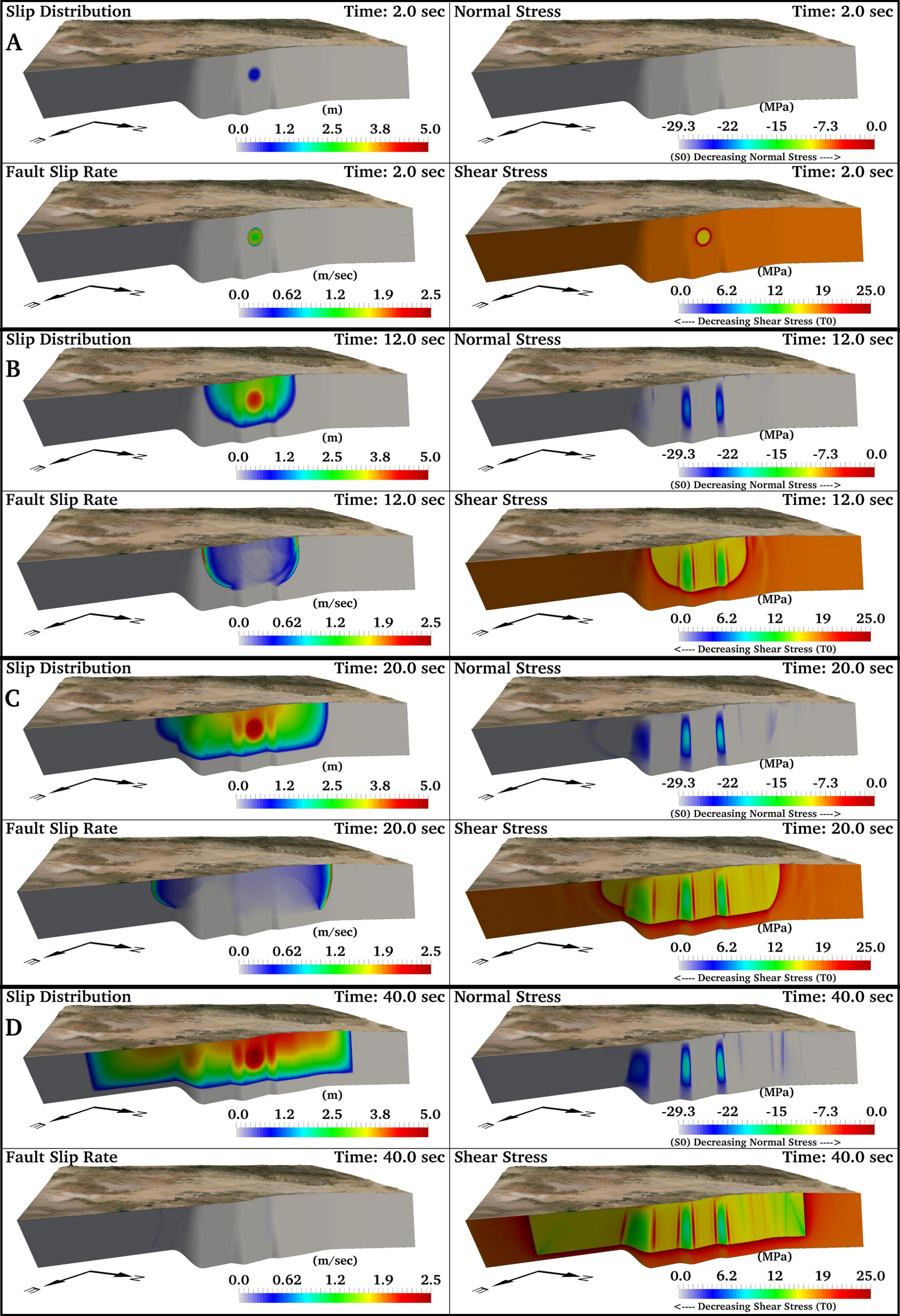
Slip Distribution
Time: 2.0 sec
A
(m)
0.0 1.2 2.5 3.8 5.0
Normal Stress
Time: 2.0 sec
(MPa)
-29.3 -22 -15 -7.3 0.0
(S0) Decreasing Normal Stress ---->
Fault Slip Rate
Time: 2.0 sec
(m/sec)
0.0 0.62 1.2 1.9 2.5
Shear Stress
Time: 2.0 sec
(MPa)
0.0 6.2 12 19 25.0
<---- Decreasing Shear Stress (T0)
Slip Distribution
Time: 12.0 sec
B
(m)
0.0 1.2 2.5 3.8 5.0
Normal Stress
Time: 12.0 sec
(MPa)
-29.3 -22 -15 -7.3 0.0
(S0) Decreasing Normal Stress ---->
Fault Slip Rate
Time: 12.0 sec
(m/sec)
0.0 0.62 1.2 1.9 2.5
Shear Stress
Time: 12.0 sec
(MPa)
0.0 6.2 12 19 25.0
<---- Decreasing Shear Stress (T0)
Slip Distribution
Time: 20.0 sec
C
(m)
0.0 1.2 2.5 3.8 5.0
Normal Stress
Time: 20.0 sec
(MPa)
-29.3 -22 -15 -7.3 0.0
(S0) Decreasing Normal Stress ---->
Fault Slip Rate
Time: 20.0 sec
(m/sec)
0.0 0.62 1.2 1.9 2.5
Shear Stress
Time: 20.0 sec
(MPa)
0.0 6.2 12 19 25.0
<---- Decreasing Shear Stress (T0)
Slip Distribution
Time: 40.0 sec
D
(m)
0.0 1.2 2.5 3.8 5.0
Normal Stress
Time: 40.0 sec
(MPa)
-29.3 -22 -15 -7.3 0.0
(S0) Decreasing Normal Stress ---->
Fault Slip Rate
Time: 40.0 sec
(m/sec)
0.0 0.62 1.2 1.9 2.5
Shear Stress
Time: 40.0 sec
(MPa)
0.0 6.2 12 19 25.0
<---- Decreasing Shear Stress (T0)

Figure 5.

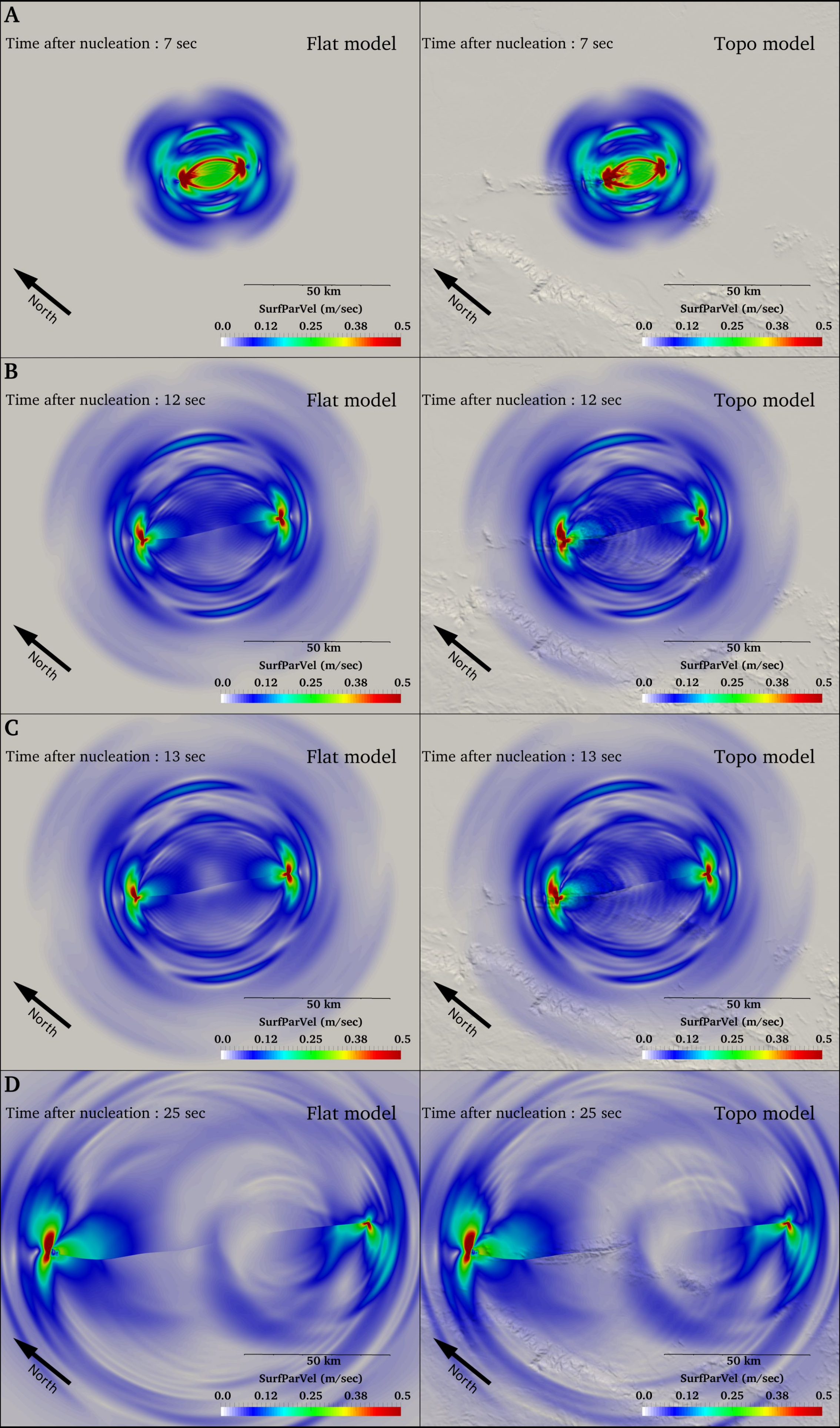
A
Time after nucleation : 7 sec
Flat model
Time after nucleation : 7 sec
Topo model
B
Time after nucleation : 12 sec
Flat model
Time after nucleation : 12 sec
Topo model
C
Time after nucleation : 13 sec
Flat model
Time after nucleation : 13 sec
Topo model
D
Time after nucleation : 25 sec
Flat model
Time after nucleation : 25 sec
Topo model
North
50 km
SurfParVel (m/sec)
0.0
0.12
0.25
0.38
0.5

Figure 6.

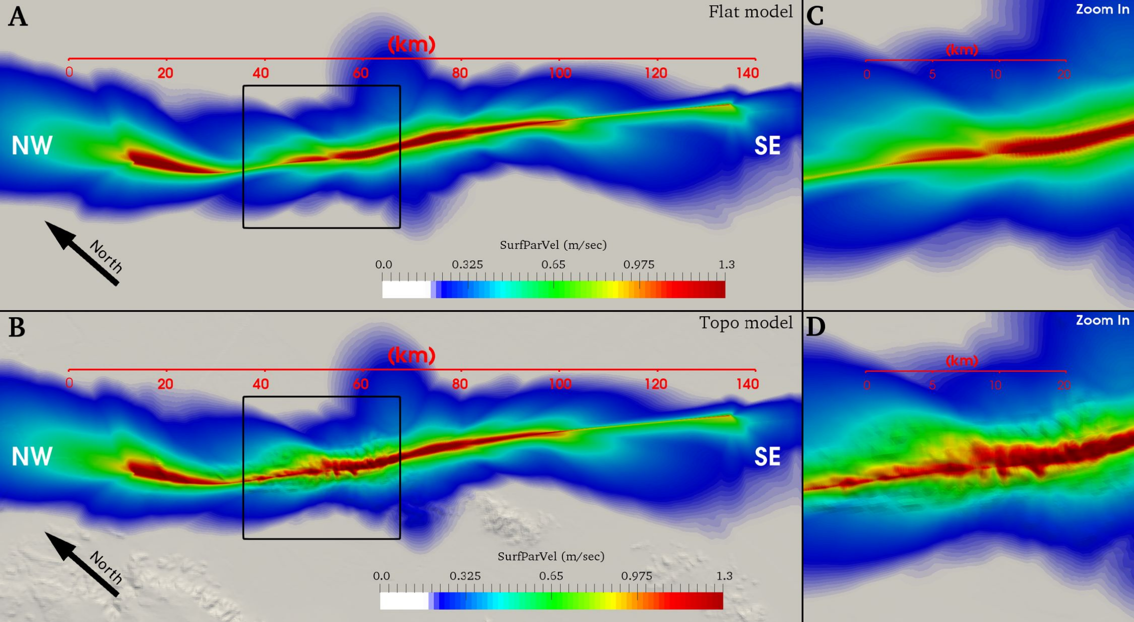
A
Flat model
(km)
0
20
40
60
80
100
120
140
NW
SE
North
SurfParVel (m/sec)
0.0
0.325
0.65
0.975
1.3
C
Zoom In
(km)
0
5
10
20
B
Topo model
(km)
0
20
40
60
80
100
120
140
NW
SE
North
SurfParVel (m/sec)
0.0
0.325
0.65
0.975
1.3
D
Zoom In
(km)
0
5
10
20

Figure 7.

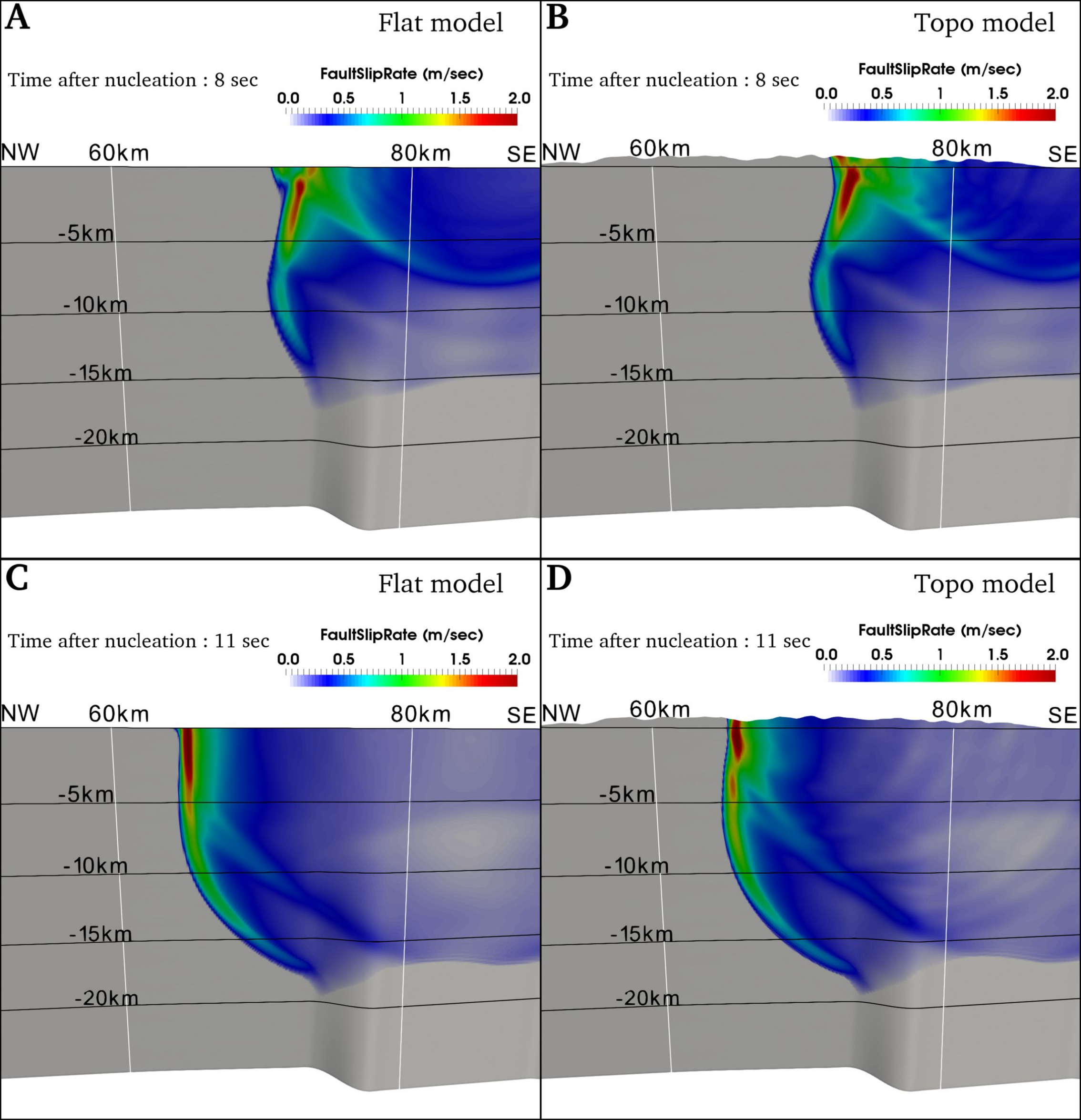
A
Flat model
Time after nucleation : 8 sec
FaultSlipRate (m/sec)
0.0 0.5 1 1.5 2.0
NW 60km 80km SE
-5km
-10km
-15km
-20km
B
Topo model
Time after nucleation : 8 sec
FaultSlipRate (m/sec)
0.0 0.5 1 1.5 2.0
NW 60km 80km SE
-5km
-10km
-15km
-20km
C
Flat model
Time after nucleation : 11 sec
FaultSlipRate (m/sec)
0.0 0.5 1 1.5 2.0
NW 60km 80km SE
-5km
-10km
-15km
-20km
D
Topo model
Time after nucleation : 11 sec
FaultSlipRate (m/sec)
0.0 0.5 1 1.5 2.0
NW 60km 80km SE
-5km
-10km
-15km
-20km

Figure 8.

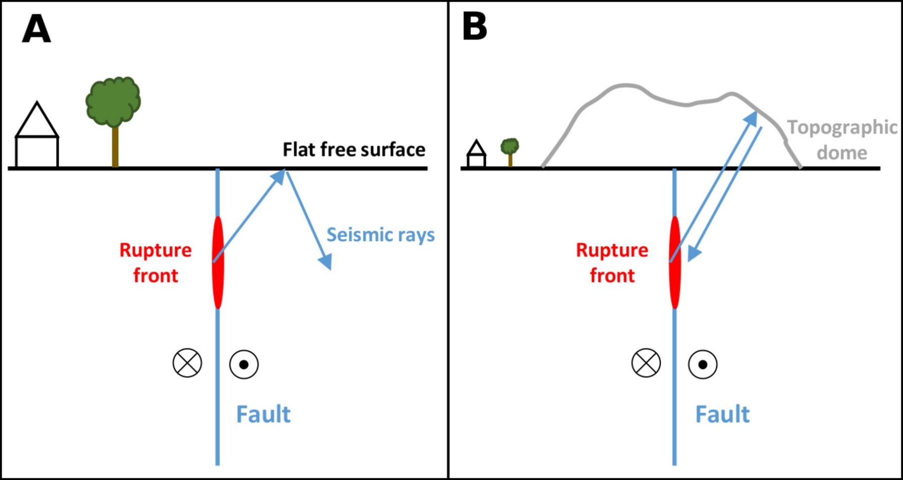
A
Flat free surface
Seismic rays
Rupture front
Fault
B
Topographic dome
Rupture front
Fault

Figure 9.

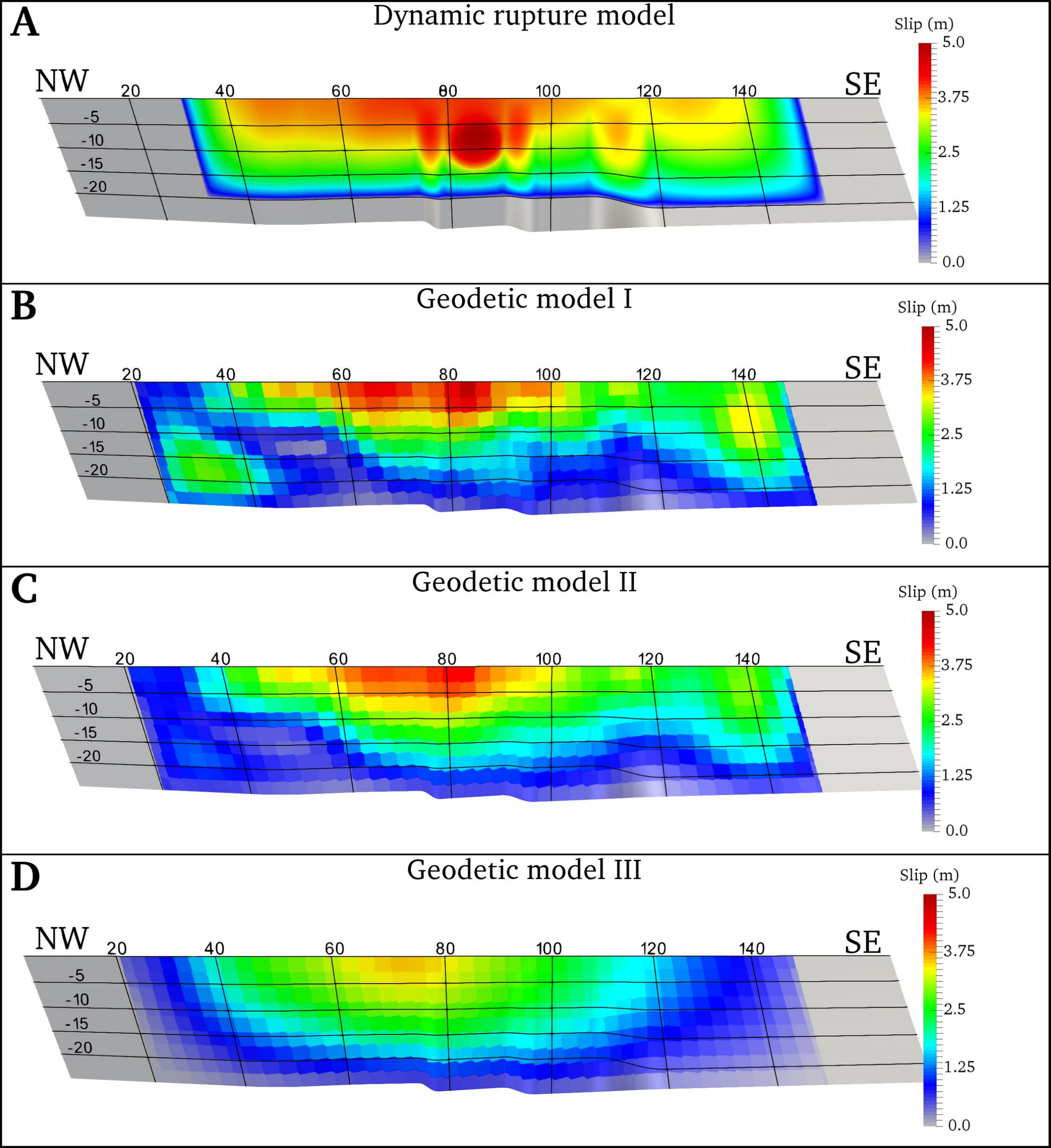
A
Dynamic rupture model
B
Geodetic model I
C
Geodetic model II
D
Geodetic model III
NW
SE
20
40
60
80
100
120
140
-5
-10
-15
-20
Slip (m)
5.0
3.75
2.5
1.25
0.0